Nearshore Vertical Pore Pressure Gradients and Onshore Sediment Transport under Tropical Storm Forcing

Matthew Florence[1]; Nina Stark, Ph.D., M.ASCE[2]; Britt Raubenheimer, Ph.D., M.ASCE[3]; and Steve Elgar, Ph.D.[4]

Abstract: Colocated sediment pore pressures at depths of approximately 0.02 and 0.22 m below the sand surface and near-bed water velocities were measured for approximately 2 weeks in approximately 1 m mean water depth on an ocean beach near Duck, North Carolina. These measurements suggest that storm wave-driven liquefaction processes may enhance local shoreward sediment transport. During the passage of tropical storm Melissa, wave heights in 26-m water depth (NDBC 44100) were 1–4 m, and storm surge (approximately 1 m) and wave-induced setup increased the water depth on the beach. Upward vertical gradients in pressure heads between the sensors increased with the storm approach, with the largest values observed before the maxima in local wave heights, wave periods, and water depths. The large gradients in pore pressure exceeded several liquefaction criteria and usually occurred when near-bed velocities were upward- and shoreward-directed. **DOI: 10.1061/(ASCE)WW.1943-5460.0000723**.

Practical Applications: Observations on an ocean beach show that during storms the water pressure below the sand surface can be greater than the pressure near the sand surface. When that difference in pressure (called a pressure gradient) becomes large, the sediments *fluidize*, that is, they act like a fluid in a process called *liquefaction*. Unlike dry or partially wet sediments, the fluidized sand is moved easily by currents. During tropical storm Melissa, large upward-directed pressure gradients fluidized the sediment, usually as the crest of an ocean wave passed over the surface. Therefore, the sediments possibly became free to move as a liquid when the currents from waves were directed both upward and toward the shore. The liquified sediments could be transported shoreward, leading to changes to the sand surface (accretion and erosion). This phenomenon is important to understand because it contributes to how, where, and when sediment might be transported on an ocean beach.

Introduction

Time-averaged cross-shore sediment transport can be difficult to quantify owing to the minute differences between on- and offshore directed transport rates (Seymour 2013). Adding to this difficulty are the many complex processes that impact cross-shore sediment transport (e.g., infiltration–exfiltration, cross-shore and upward wave-driven pressure gradients and flow accelerations, time-varying boundary layer growth, turbulence in the uprush and backwash, and drying–wetting cycles) and that change in magnitude from beach to beach (Elfrink and Baldock 2002; Amoudry and Souza 2011; Briganti et al. 2016; Chardón-Maldonado et al. 2016). Several studies suggest that interactions between the free surface flows and the flows through the sand matrix (and the associated pore pressures) have significant effects on the sediment transport in shallow water (Turner and Masselink 1998; Sleath 1999; Butt et al. 2001; Guo et al. 2019; Zhai et al. 2021). Pore pressures in sandy beach sediments have been studied in both laboratory and field settings (Yamamoto et al. 1978; Mei and Foda 1981; Sakai et al. 1992; Raubenheimer et al. 1998; Mory et al. 2007). Upward-directed pore pressure gradients (and the associated flows) reduce the sediment buoyant weight and promote sediment mobilization (Turner and Masselink 1998; Butt et al. 2001; Guo et al. 2019; Zhai et al. 2021; Stark et al. 2022). Upward gradients can be induced by exfiltration under the wave trough (Conley and Inman 1994) or by strong upward flow accelerations during collision between an incoming broken wave (bore) and the rundown from the prior wave (Pujara et al. 2015).

Large upward vertical excess pore pressure gradients within the beach can result in the mobilization of sediments, commonly referred to as momentary liquefaction (Terzaghi 1943; Sakai et al. 1992; Mory et al. 2007; Yeh and Mason 2014; Guest and Hay 2017). Here, the risk of liquefaction of the sandy sediment is quantified in three ways: (1) exceedance of the sediment buoyant weight; (2) a critical hydraulic gradient exceeding a seepage factor of safety (Terzaghi 1943; Duncan et al. 2011); and (3) a theoretical liquefaction criterion (Mory et al. 2007) at which the soil particle-to-particle contact structure changes into suspension and sediment becomes available for transport with any applied flow (Sumer 2014).

Although methods for calculating momentary liquefaction (both the in situ pressure gradients and the theoretical threshold criterion values) exist, determining the hydrodynamic or geotechnical conditions that facilitate these threshold exceeding values has proven difficult (Terzaghi 1943; Sakai et al. 1992; Mory et al. 2007; Duncan

[1]Graduate Student, Dept. of Civil and Environmental Engineering, Virginia Tech., 200 Patton Hall, Blacksburg, VA 24061 (corresponding author). ORCID: https://orcid.org/0000-0003-3876-173X. Email: matthf6@vt.edu

[2]Associate Professor, Dept. of Civil and Environmental Engineering, Virginia Tech., 200 Patton Hall, Blacksburg, VA 24061. ORCID: https://orcid.org/0000-0001-9484-069X.

[3]Senior Scientist, Woods Hole Oceanographic Institution, 266 Woods Hole Rd., Woods Hole, MA 02543.

[4]Senior Scientist, Woods Hole Oceanographic Institution, 266 Woods Hole Rd., Woods Hole, MA 02543. ORCID: https://orcid.org/0000-0001-5034-7027.

Note. This manuscript was submitted on January 13, 2022; approved on June 12, 2022; published online on September 14, 2022. Discussion period open until February 14, 2023; separate discussions must be submitted for individual papers. This paper is part of the ***Journal of Waterway, Port, Coastal, and Ocean Engineering***, © ASCE, ISSN 0733-950X.

et al. 2011; Guest and Hay 2017). The complexity of determining the hydrodynamic (e.g., wave height and period) and geotechnical (e.g., sediment bulk density and porosity) parameters arises from the difficulty in determining which parameters are relevant to momentary liquefaction and in measuring these temporally and spatially rapidly changing (i.e., significant changes on the order of seconds and centimeters for pore pressure and fluid velocities) parameters in situ without causing significant disturbance to the sediment (Yamamoto et al. 1978; Kirchner et al. 1990; Sakai et al. 1992; Mory et al. 2007; Guest and Hay 2017).

Momentary liquefaction can occur during the passage of the wave trough in partially saturated sediments (Sakai et al. 1992; Mory et al. 2007; Guest and Hay 2017). The pressure decrease resulting from the wave trough is lagged and attenuated throughout the sand column, potentially resulting in vertical pressure gradients with larger excess pore pressures deeper in the sediment than closer to the sediment–water interface.

Here, images of wave runup, combined with excess pore pressure and water velocity data collected during tropical storm Melissa (October 8–11, 2019), suggest that momentary liquefaction may also occur during the wave crest immediately following a large pressure drop from a preceding long wave trough. These events often were associated with positive horizontal (shoreward) and vertical (upward) flow velocities, suggesting a possible increase in shoreward directed sediment transport with implications for beach steepness and sediment budget calculations (Horn 2002).

Data Collection

Pore Pressure and Water Velocity Measurements

Two pressure gauges sampling at 16 Hz were inserted into the beach face shoreward of the water line during low tide on October 2, 2019, just north of the pier at the United States Army Corps of Engineers Field Research Facility (USACE-FRF) in Duck, North Carolina (Fig. 1) attached to a steel pipe approximately 0.20 m apart in the vertical [Fig. 2(a)]. The steel pipe was buried such that the topmost sensor (P_1) was approximately 0.02 m below the sand surface at the time of installation. Changes to the elevation of the sand surface owing to erosion and accretion were small during the first week of the field experiment. However, approximately 0.3 m accretion occurred during the peak of tropical storm Melissa early on October 11, 2019. Data were collected for 335 h (approximately 2 weeks) starting October 5, 2019.

Water velocity measurements were made with an acoustic doppler velocimeter (ADV) sampling at 8 Hz about 0.15 m above the bed surface [Fig. 2(a), the ADV sensor position was adjusted during daylight low tides, when possible, to maintain a roughly constant distance above the seafloor]. Velocity values with high noise-to-signal ratios were removed (Elgar et al. 2005), and cross-shore (u, positive is onshore-directed) and vertical (v, positive is upward) velocities were analyzed. The ADV measurements were upsampled via interpolation to increase the frequency to 16 Hz to compare with the pressure data.

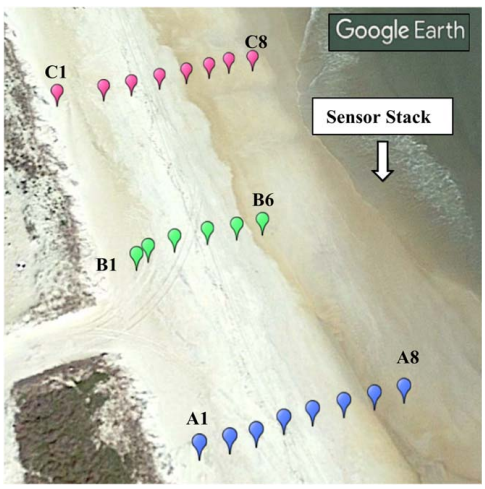

Fig. 1. Aerial view of the sensor deployment location at the USACE-FRF near low tide. Locations of sediment measurements are shown along three transects (A, B, C) separated from each other by about 35 m in the alongshore direction. The in-situ instruments were deployed about 5 m north and about 25 m offshore (east) of B6 (marked "sensor stack"). Top of the image is aligned with true north. The high-water line can be seen at stations A7, between B5 and B6, and at C5. (Map data © 2022 Google.)

Imagery

Photographs of the area surrounding the sensors were collected at 2 Hz for 9 min beginning at 15 min after each daylight hour between October 10 and 17, 2019, from a nearby five-megapixel camera. During these time periods, the images were used to corroborate wave crest arrival and the direction of surface water movement (e.g., shoreward with crest arrival). Image quality was not sufficient to check wave heights or other hydrodynamic parameters, nor could they be used to determine (subaqueous) sediment levels around the sensors as the seafloor eroded and accreted.

Clock Drift

Both attenuation and lags of the wave-induced pressure signal through porous seafloors have been observed in the field and can

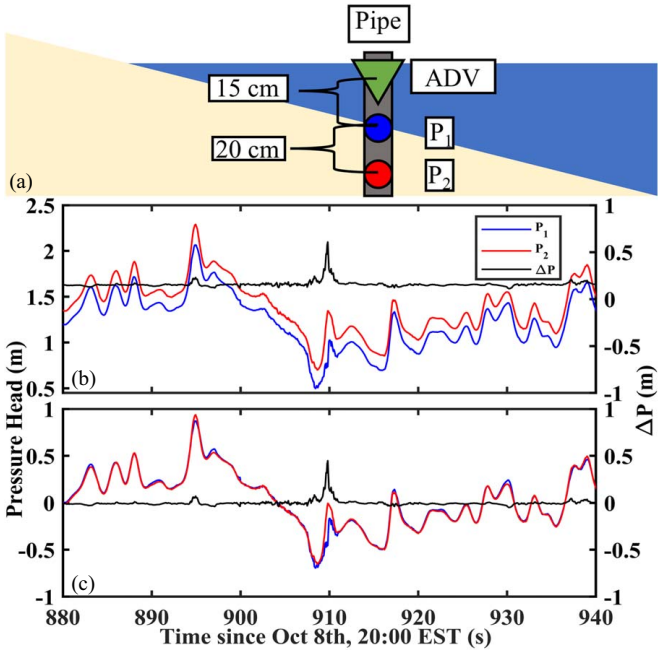

Fig. 2. (a) Sketch of sensor deployment, positions relative to the sand bed when sensors were installed; (b) phase-corrected pressure head; and (c) excess pressure head after removing still water and atmospheric pressure versus time for P_1, P_2, and their difference (ΔP).

contribute to vertical pressure gradients and momentary liquefaction (Yamamoto et al. 1978; Sakai et al. 1992; Raubenheimer et al. 1998; Mory et al. 2007; Yeh and Mason 2014; Guest and Hay 2017; Guo et al. 2019; Zhai et al. 2021; Stark et al. 2022). Small changes in the timing of pressure signals (fractions of a second) at different depths can result in large changes to the resulting vertical pressure gradients. Accurate measurements of these signal lags can be obtained with sensors synched to a common clock.

The pressure sensors used here had individual clocks that may have drifted relative to one another. Prior studies have shown the near-surface pressure signal occurs before (leads) the signal at depth (Fig. 4 in Yamamoto et al. 1978 and Fig. 10 in Guest and Hay 2017). Here, before accounting for possible clock drifts, the crests and troughs measured at the deeper location (P_2) occur before those near the bed surface (P_1) (Fig. 3).

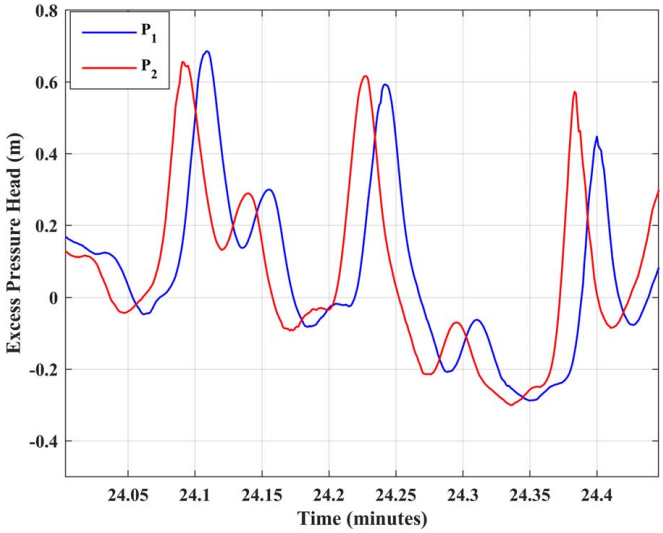

Fig. 3. Measured pore pressure signals without phase correction for P_1 (depth of 0.02 m) and P_2 (depth of 0.22 m) versus time.

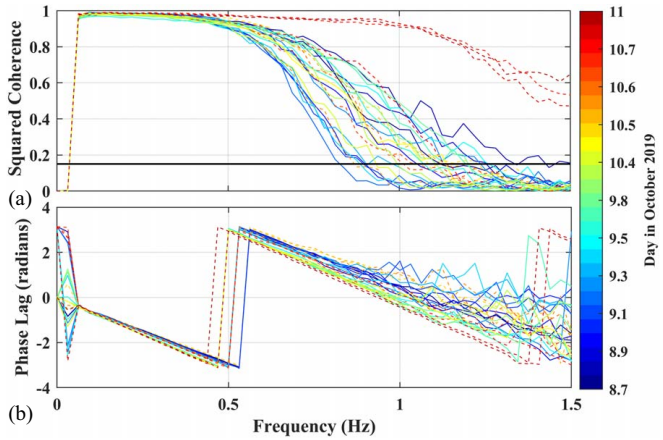

Fig. 4. (a) Squared coherence; and (b) phase lag between P_1 and P_2 (for hourly data sets with large maximum ΔP values discussed in section Liquefaction Criteria) versus frequency. The horizontal line in (a) indicates the 95% significance level (6/dof = 0.15) for 0 coherence. Note: sudden vertical jumps in lag values are due to wrapping the phase value around ± pi.

To examine the signal relationship further, cross spectra between the two pressure time series were calculated using 55,296 points (57.6 min) starting at the top of each hour with overlapping window lengths of 8,192 points and merging of three adjacent frequencies, resulting in 40 degrees of freedom. In contrast to the frequency-dependent phase shifts expected for partially saturated porous media (Yamamoto et al. 1978; Raubenheimer et al. 1998; Guest and Hay 2017), for frequencies (f) above those of infragravity waves ($f < 0.05$ Hz), phase lags increase linearly with frequency (Fig. 4), consistent with a constant time shift within each hour period. Furthermore, the phase lag at a fixed frequency increases with time [compare different curves during the month of October in Fig. 4(b)], consistent with a slowly increasing clock drift (time shift between sensors). Surge and setup were increasing as tropical storm Melissa impacted the area, and it is unlikely that saturation decreased or that the sediment properties changed to cause the increasing phase lags.

Cross-correlation was used to identify the hourly relative time shift between P_1 and P_2, which increased from 0.7 s at deployment to 1.8 s at recovery. The hour-long time series from the two pressure sensors (P_1 and P_2) were aligned (phase-corrected) to minimize the phase differences between them. The estimated vertical pressure gradients may have been affected by the removal of the estimated clock drift phase lag, which represents a source of error and uncertainty. All discussion regarding the pressure sensors and the derived results are for the phase-corrected pressure signals.

The ADV clock was synced with a different computer clock than the pressure sensors, resulting in some uncertainty when cross referencing times between the ADV and the pore pressure clocks. Therefore, the maximum velocity associated with a possible liquefaction event is the maximum velocity (either horizontal or vertical) within ±1 s of the time given by the pore pressure sensor clock. The camera clock was also set independently and was synced approximately to the pressure and ADV measurements.

Sediment Properties

Sediment samples were collected at three cross-shore transects (Fig. 1) on October 7, 9, 10, and 11, 2019, to determine porosity and relative density. Waves and swash at the location of the sensors prevented the acquisition of sediment samples with intact particle packing arrangements, and therefore, the most offshore samples (properties given in Table 1) were collected approximately 25 m onshore of the sensors. Sediment samples at A8 and C8 were collected only on October 7, 2019, due to their proximity to the water line at the time of sample collection. The values reported for B6 (Table 1) represent an average of four different samples taken on October 7, 9, 10, and 11, 2019. Properties derived from the sediment samples for all stations in the transect and for all times can be found in Table S1.

Stations A7, A8, B6, C5, C6, C7, and C8 were submerged during high tide (Fig. 1, high tide line at A7 and C5). Sediment properties

Table 1. Sediment properties of the nearest station to pressure sensors

Stations	Moisture content (%)	Degree of saturation (%)	Void ratio	Porosity	Bulk unit weight (kN/m^3)	Dry unit weight (kN/m^3)	Buoyant unit weight (kN/m^3)
A8	24.1	85.8	0.743	0.426	18.3	15.4	8.2
B6	21.2	69.1	0.740	0.420	17.7	15.5	7.6
C8	23.2	79.3	0.775	0.437	18.1	15.1	8.0

derived from samples at Stations A8, B6, and C8 are considered reasonable representations of those at the sensor location (Heathershaw et al. 1981; Kirchner et al. 1990). However, owing to the deeper water depths and longer periods of submergence, the sediment at the sensor location is expected to have a higher average moisture content and a higher unit weight (i.e., denser) compared with the estimated sediment properties (Heathershaw et al. 1981). Differences in sediment properties, water depths, and wave conditions may result in different levels of risk with respect to mobilization and transportation (Yamamoto et al. 1978; Sakai et al. 1992; Mory et al. 2007; Guo et al. 2019; Zhai et al. 2021).

Laboratory tests were not performed to estimate Poisson's ratio, sediment permeability, or the shear modulus, which are often needed in numerical models of pore pressures within the sediment bed (Yamamoto et al. 1978). However, common values of Poisson's ratio (0.33), shear modulus (4×10^{-8} Pa), and permeability (ranging between 10^{-3} and 10^{5} m/s) can be used. In the absence of laboratory tests, there are more robust calculations of sediment permeability (Carrier 2003).

Liquefaction Criteria

Three criteria were used to assess the potential for liquefaction owing to the upward pore pressure gradients that developed within the beach, including using the Mory et al. (2007) liquefaction criterion, a seepage force–derived criterion (Terzaghi 1943; Duncan et al. 2011), and a criterion for the exceedance of the sediment buoyant weight. These criteria provide calculations of liquefaction thresholds with minimal assumptions and require sediment properties (e.g., porosity, saturated, and buoyant unit weight) that are relatively straightforward to measure.

The liquefaction equation criterion (Mory et al. 2007) has been modified to compare with the values measured by the pressure sensors (i.e., a pressure head with units of meters):

$$\Delta P_{\text{crit}} = \Delta z \times \left[\left(\frac{\rho_s}{\rho_f} \right)(1-n) + n - n(C_{\text{gas}}) \left(1 - \left(\frac{\rho_g}{\rho_f} \right) \right) \right] \quad (1)$$

where ΔP_{crit} = critical pressure head difference (m) required to induce liquefaction (Mory et al. 2007); Δz = vertical distance (m) between the sensors (0.2 m); $\rho_{s,f,g}$ = density (kg/m^3) values of the sediment (2,650 kg/m^3), fluid (seawater, 1,030 kg/m^3), and gas (air, 1.225 kg/m^3), assumed to be constant; n = porosity; and C_{gas} = amount of gas within the sediment as a decimal value.

A mean ΔP_{crit} was calculated based on the mean porosity of the three closest stations, $n = 0.428$ (Table 1), the typical density values listed previously (assumed constant), a Δz of 0.2 m (assumed constant), and a range of gas contents from 0 (fully saturated) to 0.3 (30% gas content and 70% saturated) based on rounded values from Table 1, and the assumption that the offshore sediments at the sensors were at one point fully saturated. Direct measurements of gas content were not made for the sediments and were assumed based on the degree of saturation ($C_{\text{gas}} = 1 -$ degree of saturation). The corresponding mean ΔP_{crit} from Eq. (1) is 0.35 m.

The seepage force liquefaction criterion (Terzaghi 1943; Duncan et al. 2011) uses a factor of safety to assess whether a given hydraulic gradient (i) induces failure of the sediment. Here, this method of failure is momentary liquefaction induced by upward vertical pressure gradients. This criterion is determined using

$$F_e = \frac{\gamma_b}{i\gamma_{sw}} \quad (2)$$

$$i = \frac{(h_2 - h_1)}{L} \quad (3)$$

$$h_1 = \frac{P_1}{\gamma_{sw}} + z_1 + \frac{v_1^2}{2g}; \quad h_2 = \frac{P_1}{\gamma_{sw}} + z_2 + \frac{v_2^2}{2g} \quad (4)$$

$$\gamma_b = \gamma_{\text{sat}} - \gamma_{sw} \quad (5)$$

where F_e = factor of safety where failure occurs at $F_e < 1$; γ_b = sediment buoyant weight (kN/m^3); γ_{sat} = saturated sediment unit weight (kN/m^3); γ_{sw} = unit weight of seawater (10.1 kN/m^3); i = unitless hydraulic gradient; $h_{1,2}$ = corresponding hydraulic head determined via Bernoulli's equation (4) at the two sensor locations; L = unsigned distance (m) between the sensors (0.2 m, constant); $P_{1,2}$, $z_{1,2}$, and $v_{1,2}$ = respective pressure (kN/m^2), vertical position (m) with respect to a common datum, and velocity (m/s), respectively, at the measurement locations; and g = acceleration due to gravity (9.81 m/s^2).

Rearranging Eqs. (2)–(5) yields Eq. (6), which can be used to solve for the critical pressure head difference ($\Delta P_{\text{crit}} = (P_2/\gamma_{sw}) - (P_1/\gamma_{sw})$) that induces failure of the sediment:

$$\Delta P_{\text{crit}} = \frac{\gamma_b}{\gamma_{sw}} L - \Delta z - \frac{v_2^2}{2g} + \frac{v_1^2}{2g} \quad (6)$$

The distance between the sensors in this study was 0.2 m (L), and the elevations of the two sensors with respect to the sand bed were $z_1 = -0.02$ and $z_2 = -0.22$ m (negative indicating below sand bed surface). The pore fluid velocity at the P_2 sensor was assumed to be small, resulting in a small velocity head ($v_2 = 0$). An increasing velocity head at the upper sensor will increase the required pressure head difference to induce liquefaction in Eq. (6). Assuming that a v_1 of 0 m/s yields a smaller ΔP_{crit} for a worst-case scenario (i.e., the smallest ΔP required for sediment failure), the resulting ΔP_{crit} value using Eq. (6) will be 0.36 m.

The final liquefaction criterion is based on the vertical pore pressure gradient exceeding the sediment buoyant weight:

$$\Delta P_{\text{crit}} > \gamma_b \quad (7)$$

Multiplying by the distance between the sensors and the unit weight of seawater provides units consistent with the pore pressure sensor units (i.e., meters):

$$\Delta P_{\text{crit}} > \gamma_b \frac{\text{L}}{\gamma_{sw}} \quad (8)$$

From the mean bulk unit weight, constant distance between sensors, and constant unit weight of seawater, the corresponding ΔP_{crit} value is 0.16 m.

From Eqs. (1), (6), and (8), the corresponding threshold values are 0.35, 0.36, and 0.16 m, respectively. The threshold (Mory et al. 2007) used in the "Results" section was developed under similar conditions to, and may be a better representation of, the processes at this site relative to the seepage-driven liquefaction criterion (Duncan et al. 2011; Terzaghi 1943). However, the difference between the two criteria is small (2.8% difference).

Results

Pore Pressure Differences

Data collected from October 8 to 11, 2019 (long enough after the deployment time to reduce associated sediment disturbance), were analyzed to investigate the effects of tropical storm Melissa.

Pressure data were analyzed in hour-long segments, each of which was detrended to remove atmospheric and still water height pressures [including the 0.20 m vertical distance between sensors, differences in the y axes between Figs. 2(b and c)], leaving only the excess pressure head [Fig. 2(c)]. The liquefaction criteria assume that the pressure gauges P_1 and P_2 are 0.02 and 0.22 m below the sediment bed surface, respectively [Fig. 2(a)], which is roughly valid prior to October 11. Data sets were organized into three categories based on each hour-long maximum upward (positive) excess pressure head difference ($\Delta P = P_2 - P_1$) with respect to a liquefaction criterion [$\Delta P > 0.35$ m, Eq. (1) from Mory et al. 2007].

Maximum pressure head differences that meet or exceed 0.35 m (Mory et al. 2007) theoretically induce momentary liquefaction and are labeled GM. Data for which 0.28 (80% of 0.35) $< \Delta P < 0.35$ are labeled LM, indicating ΔP values that may increase the risk of momentary liquefaction but are less than the 0.35 m criterion. The 80% cutoff was chosen because it delineates between the larger (GM) ΔP values and the much smaller and more numerous ΔP values [Fig. 5(a)]. Hour-long data sets that had $\Delta P < 0.28$ m theoretically result in no liquefaction and are labeled NL. Of the 335 hour-long data sets, 18 (5.4%) were classified as GM, 9 (2.7%) were classified as LM, and 308 (91.9%) were classified as NL. The GM and LM data occurred between October 8 and 11, 2019, when local (and offshore, not shown) water levels and wave heights were increasing due to tropical storm Melissa (Fig. 5). It is possible that liquefaction was not observed following the peak of the storm owing to accretion, which resulted in sensors being buried by 0.3 to 0.5 m of sand.

In contrast to previous studies (Sakai et al. 1992; Conley and Inman 1994; Mory et al. 2007; Stark et al. 2022), excess pore pressure heads [Fig. 2(c), approximately 910 s] did not occur during wave troughs or on the back of wave crests, but instead usually occurred on the rise and peaks of wave crests. These wave crests [similar to Fig. 2(c) at approximately 910 s] occurred shortly after a significant drop in the excess pressure head [Fig. 2(c), 895–905 s, approximately 1.5 m of pressure head over 10 s], often followed by a deep trough [Fig. 2(c), approximately 907 s]. The images at the sensor location (Video S1) indicate that the water receded so that the beach surface emerged (decreasing the excess pore pressure) within about a meter of the sensors, followed by the arrival of a wave (rapidly increasing the excess pore pressure), thus causing a rapid fluctuation of the excess pore pressure within the sand column [Fig. 2(c)]. Coupled with the known attenuation of high-frequency waves at shallow depths (Yamamoto et al. 1978; Raubenheimer et al. 1998; Guest and Hay 2017), this sudden decrease and then increase of the excess pressure often caused a noticeable attenuation of the P_1 pressure signal compared with that of P_2 [Fig. 2(c), at approximately 910 s, the P_1 curve is below the P_2 curve], resulting in an upward excess pressure head difference that exceeded the failure criteria.

Pressure Head Difference Skewness and Asymmetry

Large excess pore pressure head differences were not correlated with water depth, significant wave height of sea-swell or longer period (infragravity) waves, or average wave period (Fig. 5), suggesting that other wave or sediment parameters (e.g., density, porosity, and gas content) (Yamamoto et al. 1978; Mory et al. 2007) may be important for the development of large excess pore pressure head differences. Observations gathered on a beach with similar sediment properties, but more moderate wave conditions (wave heights less than about 0.5 m) indicated small excess pore pressures following the passage of the wave crest, but did not show momentary liquefaction (Stark et al. 2022). Therefore, it is possible that high wave energy is necessary for liquefaction, but is not sufficient on its own. Time histories of geotechnical properties to determine what sediment parameters, if any, were important to the occurrence of the large excess differences were not gathered, although it is unlikely that sediment properties changed from wave to wave. In contrast, the shapes of waves did change from wave to wave. The shapes of waves and pressure gradients can be quantified by their third moments, skewness (sharp crests and flat troughs), and asymmetry (steep front faces and gently sloping rear faces) (Elgar and Guza 1985). During tropical storm Melissa (October 8–11, 2019), the maximum ΔP was not correlated with the skewness or asymmetry of P_1 or P_2 (not shown), or with the

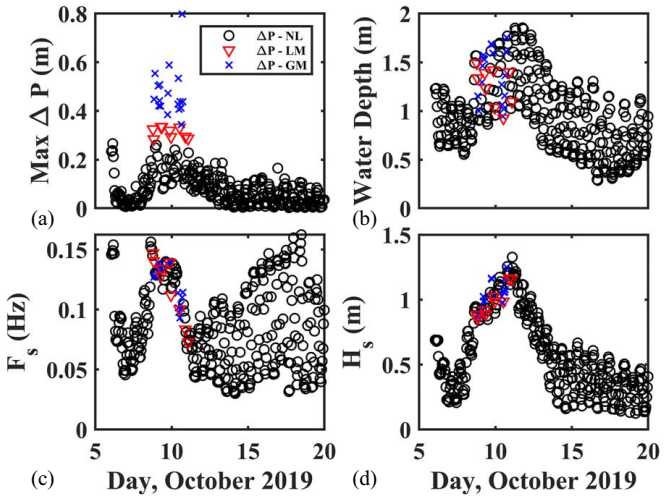

Fig. 5. (a) Maximum upward (positive) ΔP in each hour-long time series; (b) local water depth; (c) centroidal wave frequency; and (d) significant wave height estimated from observations made with the upper pressure sensor (P_1) versus time. Circle symbols are for $\Delta P < 0.28$ m, triangular symbols are for $0.28 < \Delta P < 0.35$ m, and x-symbols are for $\Delta P > 0.35$ m. Tropical storm Melissa occurred between 8 to 11 October with peak offshore (26-m water depth) waves on October 11.

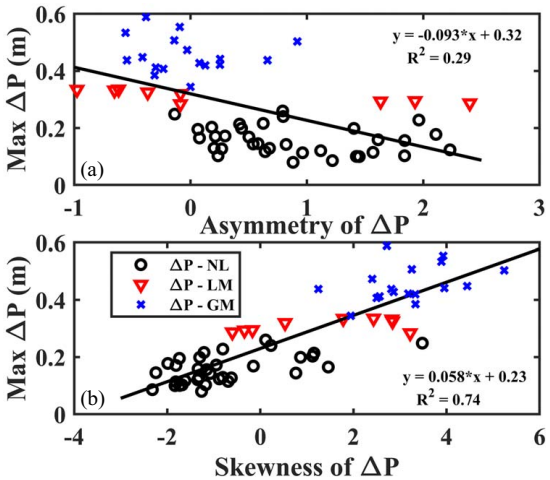

Fig. 6. The maximum ΔP for each hour-long data set versus the (a) asymmetry; and (b) skewness of ΔP. Lines are least squares fits to the data, with the fit equations and correlations (R^2) listed in each panel. Symbols refer to the maximum liquefaction threshold obtained in that hour-long data run (legend in Fig. 6b), with circle symbols for $\Delta P < 0.28$ m, triangular symbols for $0.28 < \Delta P < 0.35$ m, and x-symbols for $\Delta P > 0.35$ m.

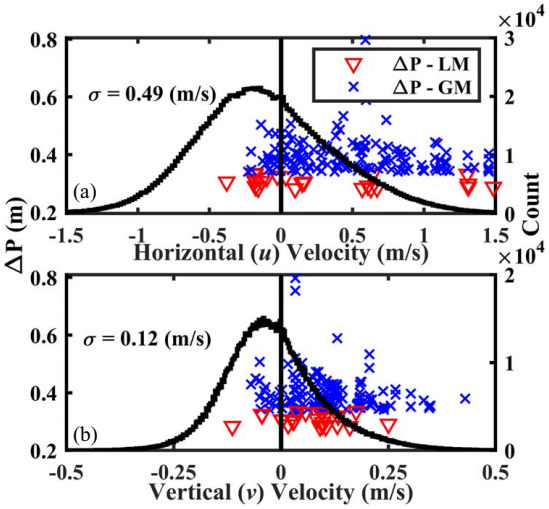

Fig. 7. Excess pore pressure gradient ΔP versus maximum (within 1 s): (a) cross-shore; and (b) vertical velocity. Positive velocity values are shoreward- and upward-directed flows, respectively. Symbols refer to the maximum liquefaction threshold obtained in that hour-long data run during tropical storm Melissa, with triangular symbols for $0.28 < \Delta P < 0.35$ m and x-symbols for $\Delta P > 0.35$ m (legend in Fig. 7a). The standard deviation σ of the velocity time series during Melissa are listed in each panel. The curves in each plot are histograms of the respective velocities (counts) during the 3-day period when the LM and GM data sets occurred (October 8–11, 2019).

asymmetry of ΔP [Fig. 6(a), $R^2 = 0.29$], but was correlated with the skewness of ΔP [Fig. 6(b), $R^2 = 0.74$]. A ΔP signal with a large positive skewness value indicates that P_2 records a larger excess pressure head than P_1 before quickly returning to values similar to those of P_1, and that the ΔP signal exhibits rapid increases and decreases followed by more quiescent periods [Figs. 2(b) and 1(c), $t = 910$ s], similar to a skewed wave with a sharp crest and broad trough.

Velocity Distributions

For the 3-day period (October 8–11, 2019) when the larger pressure gradients (LM and GM) occurred, the cross-shore and vertical velocities most often were negative (offshore and downward, Fig. 7, histogram). However, for most of the theoretical liquefaction events (Fig. 7, triangular and x symbols), both horizontal and vertical velocities observed approximately 0.15 m above the sand bed were positive (onshore- and upward-directed, respectively), suggesting that the events coincide with a shoreward propagating wave crest.

Discussion

The large ΔP values were often caused by short-lived differences in the P_1 and P_2 signals [indicated from the large R^2 for skewness of ΔP, Fig. 5(b)] arising from a rapid increase and then a decrease in the pressure values. These large excess differences almost always occurred when a wave crest passed over the sensors [e.g., Figs. 2(b) and 1(c), $t = 910$ s and positive u in Fig. 7] immediately after a significant decrease in the pore pressure head [Figs. 2(b and c), $t = 900$–908 s]. For all theoretical liquefaction events recorded simultaneously with image sequences (one example shown in Video S1), the spike in ΔP occurred during a significant recession [e.g., pressure head of 0.9 to −0.6 m in 10 s, Fig. 2(b), $895 < t < 905$ s P_1 and P_2 curves] of the waves and water line (a significant reduction in the over-sensor water depth) that was followed by a wave crest and the return of the water line. The pressure drop [Figs. 2(b and c), $900 < t < 908$ s] most likely was caused by the rapid seaward movement of water away from the sensors, which may have caused exfiltration of pore water. The rapid return of the water, coupled with the increased pressure from the arriving wave crest, likely caused the sudden jump in pore pressure [e.g., Figs. 2(b and c) at $t = 910$ s]. The observed flows and pressure gradients during the liquefaction events have similarities with those observed in the laboratory owing to interactions between a solitary wave and the rundown from a prior wave (Pujara et al. 2015; e.g., see the discussion of Fig. 16). In some cases, the near-bed flows were offshore-directed even as the wave crest moved onshore past the sensors, suggesting large shear in the flows (Video S1).

With the sediment becoming liquefied during shoreward and upward directed fluid velocities (Fig. 7), it is possible that the sediment was transported shoreward as suspended load, resulting in shoreward deposition of sediments coinciding with the arrival of the wave crests, consistent with laboratory results (Madsen 1974; Packwood and Peregrine 1979). In-bed pore flow (comparable to the measurements of ΔP here) caused the bed to be unable to resist additional forces (i.e., liquified the bed) (Madsen 1974), and the upward velocity after the wave [e.g., Fig. 7(b)] would cause the liquified bed sand to be entrained in the fluid flow (Packwood and Peregrine 1979).

Conclusions

Sandy sediment pore pressures vertically separated by 0.2 m and near-bed water velocities were measured in about 1 m water depth on an ocean beach for approximately 2 weeks in October 2019. During tropical storm Melissa (October 8–11, 2019), excess pressure head differences (ΔP) exceeded sediment momentary liquefaction criteria. These criteria-exceeding values occurred as the storm-driven waves and water depth increased, but ΔP was not correlated with wave height, wave period, water depth, or near-bed cross-shore velocity. Often, a large ΔP occurred soon after the water level receded during a large wave trough, causing a strong reduction in the excess pressure head and as a returning wave crest caused a rapid increase in the pore pressure. The maximum ΔP value in an hour-long data set increased and was correlated with the skewness of the hour-long ΔP signal. Excess pore pressure heads often occurred during onshore-and upward-directed orbital velocities and therefore can result in onshore transport of suspended liquefied sediments.

Data Availability Statement

All data, models, or code that support the findings of this study are available from the corresponding author upon reasonable request. The data can also be found in an online DesignSafe repository, https://doi.org/10.17603/ds2-g5dk-7548, under PRJ-3381v2/Field Data/North Carolina/DUNEX 2019. The data in the repository contain the pressure, ADV, and location of the sensor data.

Acknowledgments

We thank the staff of the U.S. Army Engineer Research and Development Center Field Research Facility, Levi Gorrell for providing logistical and field support, and Brittany Bruder for providing and assisting with the sea state images. We thank the U.S. Coastal Research Program (USCRP) for its coordination and facilitation of the During Nearshore Event Experiment (DUNEX). Research funding was provided

by the National Science Foundation (awards CMMI-1751463, OCE-1829136, OCE-1848650, and OCE-1933010), the USCRP, and a Vannevar Bush Faculty Fellowship. The authors declare no financial or other conflicts of interest.

Supplemental Materials

Table S1 and Video S1 are available online in the ASCE Library (www.ascelibrary.org).

References

Amoudry, L. O., and A. J. Souza. 2011. "Deterministic coastal morphological and sediment transport modeling: A review and discussion." *Rev. Geophys.* 49 (2): 1–21. https://doi.org/10.1029/2010RG000341.

Briganti, R., A. Torres-Freyermuth, T. E. Baldock, M. Brocchini, N. Dodd, T. J. Hsu, J. Zhonglian, K. Yeulwoo, J. C. Pintado-Patino, and M. Postacchini. 2016. "Advances in numerical modelling of swash zone dynamics." *Coastal Eng.* 115: 26–41. https://doi.org/10.1016/j.coastaleng.2016.05.001.

Butt, T., P. Russell, and I. Turner. 2001. "The influence of swash infiltration–exfiltration on beach face sediment transport: Onshore or offshore?" *Coastal Eng.* 42 (1): 35–52. https://doi.org/10.1016/S0378-3839(00)00046-6.

Carrier, W. D., III 2003. "Goodbye, Hazen; Hello, Kozeny–Carman." *J. Geotech. Geoenviron. Eng.* 129 (11): 1054–1056. https://doi.org/10.1061/(ASCE)1090-0241(2003)129:11(1054).

Chardón-Maldonado, P., J. C. Pintado-Patiño, and J. A. Puleo. 2016. "Advances in swash-zone research: Small-scale hydrodynamic and sediment transport processes." *Coastal Eng.* 115: 8–25. https://doi.org/10.1016/j.coastaleng.2015.10.008.

Conley, D. C., and D. L. Inman. 1994. "Ventilated oscillatory boundary layers." *J. Fluid Mech.* 273: 261–284. https://doi.org/10.1017/S002211209400193X.

Duncan, J. M., B. O'Neil, T. Brandon, and D. R. VandenBerge. 2011. Vol. 64 of *Evaluation of potential for erosion in levees and levee foundations*, 1–40. Blacksburg, VA: Center for Geotechnical Practice and Research.

Elfrink, B., and T. Baldock. 2002. "Hydrodynamics and sediment transport in the swash zone: A review and perspectives." *Coastal Eng.* 45 (3–4): 149–167. https://doi.org/10.1016/S0378-3839(02)00032-7.

Elgar, S., and R. T. Guza. 1985. "Observations of bispectra of shoaling surface gravity waves." *J. Fluid Mech.* 161: 425–448. https://doi.org/10.1017/S0022112085003007.

Elgar, S., B. Raubenheimer, and R. T. Guza. 2005. "Quality control of acoustic Doppler velocimeter data in the surfzone." *Meas. Sci. Technol.* 16 (10): 1889. https://doi.org/10.1088/0957-0233/16/10/002.

Guest, T. B., and A. E. Hay. 2017. "Vertical structure of pore pressure under surface gravity waves on a steep, megatidal, mixed sand-gravel-cobble beach." *J. Geophys. Res.: Oceans* 122 (1): 153–170. https://doi.org/10.1002/2016JC012257.

Guo, Z., D.-S. Jeng, H. Zhao, W. Guo, and L. Wang. 2019. "Effect of seepage flow on sediment incipient motion around a free spanning pipeline." *Coastal Eng.* 143: 50–62. https://doi.org/10.1016/j.coastaleng.2018.10.012.

Heathershaw, A. D., A. P. Carr, M. W. L. Blackley, and C. F. Wooldridge. 1981. "Tidal variations in the compaction of beach sediments." *Mar. Geol.* 41: 223–238. https://doi.org/10.1016/0025-3227(81)90082-7.

Horn, D. 2002. "Beach groundwater dynamics." *Geomorphology* 48: 121–146. https://doi.org/10.1016/S0169-555X(02)00178-2.

Kirchner, J. W., W. E. Dietrich, F. Iseya, and H. Ikeda. 1990. "The variability of critical shear stress, friction angle, and grain protrusion in water-worked sediments." *Sedimentology* 37: 647–672. https://doi.org/10.1111/j.1365-3091.1990.tb00627.x.

Madsen, O. S. 1974. "Stability of a sand bed under breaking waves." *Coastal Eng. Proc.* 1 (14): 45. https://doi.org/10.9753/icce.v14.45.

Mei, C. C., and M. A. Foda. 1981. "Wave-induced responses in a fluid-filled poroelastic solid with a free surface: A boundary layer theory." *Geophys. J. Int.* 66 (3): 597–631. https://doi.org/10.1111/j.1365-246X.1981.tb04892.x.

Mory, M., H. Michallet, D. Bonjean, I. Piedra-Cueva, J. M. Barnoud, P. Foray, S. Abadie, and P. Breul. 2007. "A field study of momentary liquefaction caused by waves around a coastal structure." *J. Waterway, Port, Coastal, Ocean Eng.* 133 (1): 28–38. https://doi.org/10.1061/(ASCE)0733-950X(2007)133:1(28).

Packwood, A. R., and D. H. Peregrine. 1979. "The propagation of solitary waves and bores over a porous bed." *Coastal Eng.* 3: 221–242. https://doi.org/10.1016/0378-3839(79)90022-X.

Pujara, N., P. L.-F. Liu, and H. H. Yeh. 2015. "An experimental study of the interaction of two successive solitary waves in the swash: A strongly interacting case and a weakly interacting case." *Coastal Eng.* 105: 66–74. https://doi.org/10.1016/j.coastaleng.2015.07.011.

Raubenheimer, B., S. Elgar, and R. Guza. 1998. "Estimating wave heights from pressure measured in sand bed." *J. Waterway, Port, Coastal, Ocean Eng.* 124 (3): 151–154. https://doi.org/10.1061/(ASCE)0733-950X(1998)124:3(151).

Sakai, T., K. Hatanaka, and H. Mase. 1992. "Wave-induced effective stress in seabed and its momentary liquefaction." *J. Waterway, Port, Coastal, Ocean Eng.* 118 (2): 202–206. https://doi.org/10.1061/(ASCE)0733-950X(1992)118:2(202).

Seymour, R. 2013. *Nearshore sediment transport*. 1st ed. New York: Springer.

Sleath, J. F. A. 1999. "Conditions for plug formation in oscillatory flow." *Cont. Shelf Res.* 19: 1643–1664. https://doi.org/10.1016/S0278-4343(98)00096-X.

Stark, N., P. Mewis, B. Reeve, M. Florence, J. Piller, and J. Simon. 2022. "Vertical pore pressure variations and geotechnical sediment properties at a sandy beach." *Coastal Eng.* 172: 104058. https://doi.org/10.1016/j.coastaleng.2021.104058.

Sumer, M. 2014. *Liquefaction around marine structures*. 1st ed. Singapore: World Scientific.

Terzaghi, K. 1943. *Theoretical soil mechanics*. New York: Wiley.

Turner, I. L., and G. Masselink. 1998. "Swash infiltration–exfiltration and sediment transport." *J. Geophys. Res.: Oceans* 103 (C13): 30813–30824. https://doi.org/10.1029/98JC02606.

Yamamoto, T., H. L. Koning, H. Sellmeijer, and E. van Hijum. 1978. "On the response of a poro-elastic bed to water waves." *J. Fluid Mech.* 87 (1): 193–206. https://doi.org/10.1017/S0022112078003006.

Yeh, H., and H. B. Mason. 2014. "Sediment response to tsunami loading: Mechanisms and estimates." *Géotechnique* 64 (2): 131–143. https://doi.org/10.1680/geot.13.P.033.

Zhai, H., D.-S. Jeng, Z. Guo, and Z. Liang. 2021. "Impact of two-dimensional seepage flow on sediment incipient motion under waves." *Appl. Ocean Res.* 108: 102510. https://doi.org/10.1016/j.apor.2020.102510.